



# High load carrying structures made from folded composite materials

Arthur Schlothauer\*, Urban Fasel, Dominic Keidel, Paolo Ermanni

CMASLab, ETH Zurich, Leonhardstrasse 21, 8092 Zurich, Switzerland



## ARTICLE INFO

### Keywords:

Foldable structures  
Thin shell composites  
Composite design  
Composite manufacturing  
Additive manufacturing  
Optimization

## ABSTRACT

Large design and manufacturing effort for high load carrying composite structures results from anisotropic material behavior, tedious curing or forming conditions as well as high sensitivity to manufacturing defects. Such challenges limit the design freedom and result in large cost and time effort. A novel design approach is proposed to realize load carrying structures based on the utilization of the outstanding flexibility of thin composite shells and the “complexity for free” approach of additive manufacturing. To this purpose, highly integrated structures are created by folding cured and thin composite shells around additively manufactured internal core topologies. The developed structures do not require complex molding approaches, while maintaining a high degree of manufacturing quality. A multidisciplinary design optimization is used to fully exploit the design freedom and the load carrying capabilities of the structure. Following the design concept, a UAV wing structure that carries more than 100 times its own weight is developed, optimized and tested to validate the design approach and demonstrate load carrying ability and manufacturing quality.

## 1. Introduction

Design and manufacturing effort of lightweight composite structures increases drastically with increasing demand on load carrying capability [1,2]. Especially high performance structures, utilized for example in aerospace applications, have highest demands on manufacturing quality. This is accompanied by large manufacturing cost and time effort and leads to long lead times and slow design iterations. To the contrary, rapid prototyping approaches gained increasing interests over the years and can also improve the design process of novel rapidly growing industries like the drone market [3], airborne wind energy [4] or small VTOL passenger aircraft [5,6]. Processes like additive manufacturing with its capability to quickly produce complex geometries already show potential in facilitating novel designs [7]. However, they are not yet applicable to large load carrying structures and hence not an alternative to mold-based approaches, which are required to yield good mechanical properties for high performance applications. Recent developments in continuous fiber 3D-printing with high volume fractions are promising to overcome this chasm [8,9], but still require a considerable amount of development to produce the highest complexity parts at aerospace quality.

The herein proposed design approach and manufacturing concept leverages both, the “complexity for free” approach of additive manufacturing as well as the high load carrying capability of conventionally

manufactured carbon fiber reinforced polymer (CFRP) shells. However, it does not require complex tooling mechanisms for the composite parts and instead uses a principle common to ship building and architecture [10]. For this purpose, the theory of developable surfaces is utilized to bend flat and thin locally reinforced composite skins around additively manufactured internal structures (cores). The multifunctional cores serve as skin reinforcement (ribs) and shape giving geometry. Inspired by deployable space structures, which use folded composite shells for the efficient stowage of load carrying structures in a launcher vehicle [11,12], the critical bending radii of the composite shells are tested to predict feasible shapes realizable by the novel folding technique. The concept of the design approach is shown in Fig. 1. Based on the example of a highly load carrying UAV-wing, feasible wing geometries are investigated. To demonstrate that the novel concept is suitable for high load carrying lightweight structures, a multidisciplinary design optimization is utilized to create a UAV-Wing that withstands loads of more than 100 times its own weight, considering the constraints imposed by the foldability of the structure. To verify the proposed concept and to show that folded structures can be designed using classical numeric calculation approaches, the wing is manufactured, tested and compared to finite element predictions.

The aim of this work is to introduce a novel structural design and manufacturing concept, that bridges the gap between a state-of-the-art high performance composite structure that underwent a time and

\* Corresponding author.

E-mail address: [arthursc@ethz.ch](mailto:arthursc@ethz.ch) (A. Schlothauer).

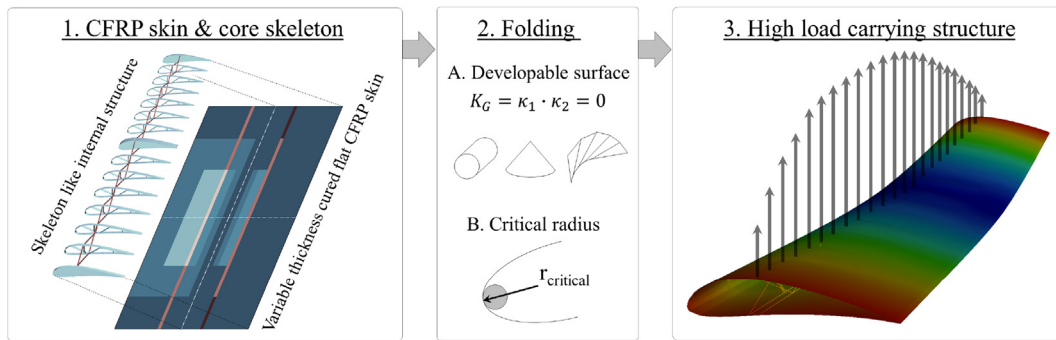


Fig. 1. Design approach: 1. Manufacturing of the skeleton like internal core structure and variable thickness flat composite skin. 2. Folding and bonding the skin onto the internal structure, considering the critical folding radius of thin composites and the use of developable surfaces. 3. Achieve high load carrying structure.

cost intensive manufacturing process, and a fully additively manufactured structure that enables quick and cost efficient design iterations, geometric complexity and function integration, but lacks the required load carrying ability and manufacturing quality. Furthermore, this work reveals potential and limits of folded composite structures for high-performance structural application and validates this concept with regard to shape accuracy, manufacturing quality and load carrying capabilities.

## 2. Materials and methods

To realize shapes folded by shear stiff materials like cured carbon fiber composite skins, the gaussian curvature (Eq. (1)), which describes the product of the two principal curvatures, has to be zero at any point.

$$K_G = \kappa_1 \cdot \kappa_2 = 0 \quad (1)$$

Surfaces with these intrinsic properties are called developable surfaces. Every surface that can be flattened onto a planar surface without creasing, tearing or stretching is a developable surfaces [13]. Although being limited to a flat sheet, the theory for developable surfaces allows to construct a wide range of geometries through pure bending of the sheet. There are three classes of developable surface (conical, cylindrical and tangential) which can be combined to lead to an efficient design of functional structures in the textile industry, architecture or ship-building [10,14]. The construction of such structures is well studied and relies on combination of developable surfaces [15,16] or the minimization of gaussian curvature in the parent class of the developable surfaces, so called ruled-surfaces [14]. The theory of developable surfaces that are subjected to folding loads is successfully applied to thin composite shells in space structures, where the low forming forces associated with developable surfaces are utilized to efficiently package stiff structures into the limited volume of a launcher vehicle [17]. This study further extends the ability to form complex geometric and load carrying structures out of thin composite shells and uses it for the direct manufacturing of a high load carrying wing.

To verify the feasible scale and geometrical limitations, large deformation platen folding tests [18] need to be conducted. The test allows to estimate required folding moments and constraining maximum bending curvatures to form the desired geometrical shapes. The large deformation platen folding test, commonly used in foldable space structure design, therefore allows to extract critical bending radii of the material as well as the required folding forces per unit length to shape the material to an observed curvature.

In the platen test, two aluminum platens travel towards each other with a speed of 20 mm/min. The movement of the platens buckles a thin specimen, which is vertically attached to the edge of the platens, shown in Fig. 2. The specimen is initially fixed with adhesive tape to the edge of the platen to prevent it from slipping after initial buckling.

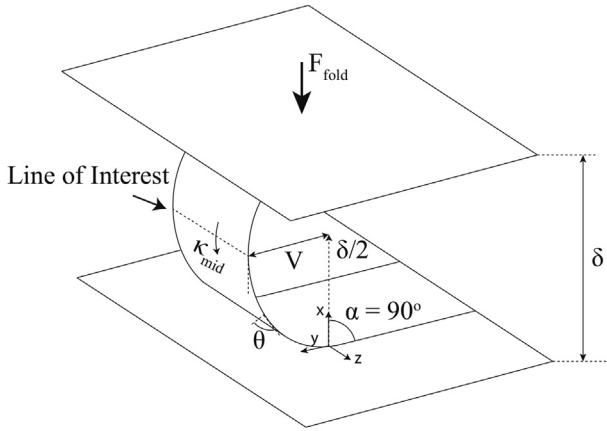


Fig. 2. Large deformation platen test setup showing DIC and testing machine configurations.

Platen separation ( $\delta$ ) and folding forces ( $F_{\text{fold}}$ ) are recorded with a Zwick Roell testing machine. Specimen curvature ( $\kappa$ ) and surface strains ( $\epsilon$ ) are recorded with a digital image correlation system (DIC), which is synchronized with the measured data from the Zwick testing machine. Fig. 3 shows the most important parameters of the platen test.

The test is conducted on woven Tencate TC-250 carbon fiber pre-pregs of varying thickness (From one to four plies, thickness investigated in a Keyence VHX6000 optical microscope). As the layup of the wing skin contributes significantly to the torsional stiffness of the wing, the bending tests are limited to  $\pm 45$  degrees layups as this will maximize the torsional stiffness and minimize the required bending forces for the forming of the wing skin. The samples are cut out of a flat laminated plate of the investigated material, which is cured at 130 °C and 3 bar pressure in an autoclave. For each thickness, seven samples are investigated. Specimen dimensions are chosen to 120 mm  $\times$  40 mm to reduce edge effects during the platen tests. A thin layer of acrylic paint is applied on the surface of the specimens to improve contrast between the applied speckles and the surface, reducing measuring noise in the large deformation digital image correlation analysis [19]. The results are analyzed using the commercial Vic3D tool.

For an estimation of the required folding moments to achieve the introduced airfoil geometries, one can calculate the resulting moments from the platen test. Therefore, the measured folding force and corresponding curvature are implemented into the theory of Eulers elastica [20] following the example of Sanford et al. [21]. The large deformation of elastically buckled bars allows to correlate the true curvature  $\frac{d^2y}{ds}$  (It shall be noted, that the large deformation analysis requires the true curvature and not the approximate curvature defined as  $\frac{d^2y}{dx^2}$ ) of the sample with a given platen force by:



**Fig. 3.** A schematic illustrating the most important parameters in the platen test: Platen separation  $\delta$ , platen force  $F_{\text{fold}}$ , mid-line curvature  $\kappa$ , the deformation angle  $\theta$ , the boundary angle  $\alpha$  as well as distance between sample tangency points and line of interest  $V$ .

$$EI \cdot \frac{d\theta}{ds} = -F_{\text{fold}} \cdot y \quad (2)$$

Neglecting the change in length of the specimen due to compression, the length  $l$  of the curved part of the sample can be calculated for every given tip deflection angle  $\alpha$ , using a first complete elliptic integral  $K(p)$  (for a derivation the reader is referred to Timoshenko's work [20]):

$$l = \frac{1}{k} \cdot \int_0^{\pi/2} \frac{d\phi}{\sqrt{1-p^2 \sin^2(\phi)}} = \frac{1}{k} \cdot K(p) \quad (3)$$

with

$$k = \sqrt{\frac{F_{\text{fold}}}{EI}} \quad (4)$$

$$p = \sin\left(\frac{\alpha}{2}\right) \quad (5)$$

and introducing the variable  $\phi$  such that:

$$\sin\left(\frac{\theta}{2}\right) = \sin\left(\frac{\alpha}{2}\right) \cdot \sin(\phi) \quad (6)$$

Once tangency of the sample with the platens is established ( $\alpha = 90^\circ$ ), the deflection curve of the elastica is known as

$$y = \frac{2p}{k} \cdot \int_0^{\pi/2} \sin(\phi) d\phi = \frac{2p}{k} \quad (7)$$

and

$$x = \frac{2}{k} \cdot \int_0^{\pi/2} \sqrt{1-p^2 \sin^2(\phi)} d\phi - l = \frac{2}{k} \cdot E(p) - l \quad (8)$$

according to Ref. [20].

The tabulated values for the second complete elliptic integral  $E(p)$  (Eq. (8)), as well as for  $K(p)$  (Eq. (3)) allow for the determination of the ratio  $\frac{x}{l} = 0.457$  and  $\frac{y}{l} = 0.763$  for  $\alpha = 90^\circ$ . At the critical point of highest curvature  $x = \frac{\delta}{2}$  one can calculate  $V = y(x = \frac{\delta}{2})$  using these ratios resulting in a correlation between folding moment  $M = F_{\text{fold}} \cdot V$  as:

$$M = 1.6693 \cdot F_{\text{fold}} \cdot \frac{\delta}{2} \quad (9)$$

Considering these requirements, high load carrying structures can be designed such that they comply with the limitations of the structural and manufacturing concept regarding minimum folding radius and the use of developable surfaces. For demonstration purposes, this study will investigate solely cylindrical developable shells with constant cross

section. However, also more complex shells with varying cross section have been shown to be assembled from developable surfaces [15].

### 3. Structural concept

The structure investigated in this study is a UAV wing consisting of a folded CFRP skin and an additively manufactured truss like internal structure. The internal structure is made from polylactide (PLA) ribs and CFRP rods, replacing conventional ribs and spars. The wing structural concept is shown in Fig. 4. The CFRP wing skin with variable layup and unidirectional (UD) spar caps is laminated and cured on a flat surface. The cured wing skin is folded around and bonded onto the shape-defining ribs. Additionally to providing the stiffness in chordwise direction and decreasing the shear forces limiting buckling in the wing skin, the ribs also function as shape-giving manufacturing mold of the wing. The ribs are interconnected through CFRP rods in alternating orientation to transfer shear forces between the spar caps, defining a skeleton like internal structure.

As the thickness of the wing skin is expected to be low to comply with the folding constraints, the design of the structure has to account for structural and aeroelastic effects like buckling, excessive wing twist and flutter that may limit the load carrying capability of the wing. To exclude these effects and to show the maximum achievable performance with respect to sustainable load factors, a numerical optimization considering aeroelastic interactions is performed. A parametrized aeroelastic model of the wing<sup>1</sup> [22,23] is therefore embedded in an evolutionary algorithm based optimization [24], allowing to find optimized structural designs in terms of load carrying capability by fulfilling aerostructural requirements. This includes wing twisting, buckling and flutter constraints. Buckling loads are assessed conducting a linear static buckling analysis using Nastran [25], whereas the flutter speed is assessed based on the assumption of stationary aerodynamics and assumed mode shapes [26,27]. Simultaneously, wing skin folding constraints, which are given by the large deformation material testing, are considered by applying a safety factor of  $\geq 3$  to limit non-linear material effects like matrix yielding, micro-cracking or non-linear carbon fiber behaviour (accompanied at large folding strains [18]).

Within the optimization, the optimizer is free to vary a large number of design variables, collected in Table 1. The parameters can be divided in two main groups: the structural parameters and the composite layup thickness parameters. The structural parameters are the number of ribs  $N_{\text{ribs}}$ , the chordwise position of the two spars  $x_{\text{spar}}$  (defining the position and width of the spar caps), the spar rod radius  $r_{\text{rods}}$  (linearly varying in spanwise direction), and the Voronoi graph-based parameters of the truss structure of the rib  $x_V$ ,  $y_V$ ,  $t_V$  [28]. A Voronoi parametrization is used for the UAV wing truss-structure design [22,29,30], as the number of parameters is small, the structure has no unconnected segments and small changes in parameters lead to small changes in shape. With respect to the aeroelastic characteristics, the "complexity for free" principle of the additively manufactured ribs allows for accurate tuning of the deformation behaviour to comply with the buckling and twist constraints. In terms of composite layup, the layup orientation is predefined, whereas the number of layers is free to vary. A base  $45^\circ$  CFRP twill layer covers the full wing and ensures a closed profile. The wing is divided into eight spanwise sections and four chordwise sections, resulting in 64 sectors for the top and bottom skin. The optimizer can place additional  $45^\circ$  twill layers in these sectors to reinforce the structure. The parameter space in the optimization is continuous, defined as the number of layers of the laminate  $t_{\text{Twill}}$ . To guarantee manufacturability of the optimized layup, the number of layers is rounded to the next integer to define

<sup>1</sup> The underlying aeroelastic model consists of a two-way coupled fluid structure interaction (FSI) simulation, coupling a detailed shell and beam element based finite element model with a 3D panel method based aerodynamic model.

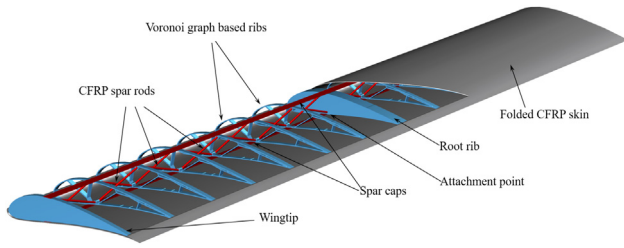


Fig. 4. Wing structural concept.

Table 1  
Wing optimization parameters.

Design parameters DP		#DP	
Structure	Number of ribs	$N_{ribs}$	1
	Voronoi X-, Y-position	$x_V, y_V$	24
	Voronoi thickness	$t_V$	12
	Spar chord-positions	$x_{spar}$	2
	Spar rod radius	$r_{rods}$	2
Thickness	Unidirectional	$t_{UD}$	16
	Twill	$t_{Twill}$	64
Total			121

an exact number of layers before generating the finite element model of the wing structure within the optimization. Additionally, the number of CFRP UD layers  $t_{UD}$  in the top and bottom spar cap can be varied by the optimizer. To guarantee the foldability of the structure, constraints are imposed on the maximum number of layers as a function of the local curvature of the wing. This especially applies to the leading edge region of the wing, where the maximum curvature is observed. The material choice and properties can be found in Table 2.

The mathematical formulation of the optimization can be found in Eq. (10). The objective is to maximize the ratio of acting lift forces to structural weight ( $\frac{F_{Lift}}{mg}$ ), considering the constraints imposed by folding ( $R_{crit}$ ), flutter ( $V_{flutter}$ ), buckling ( $k_b$ ) and wing twisting ( $\theta_{wing}$ ) at a theoretical maximum flight speed of  $V_{max} = 50$  m/s and angle of attack of  $\alpha = 8^\circ$ .

$$\begin{aligned}
 &\text{minimize } \mathbf{f}(\mathbf{x}) = -\frac{F_{Lift}}{mg}(\mathbf{x}) & \mathbf{x} \in \mathbb{R}^{121} \\
 &\text{subject to } \mathbf{x}_{low} \leq \mathbf{x} \leq \mathbf{x}_{up} & \mathbf{x}_{low}, \mathbf{x}_{up} \in \mathbb{R}^{121} \\
 &\mathbf{g}(\mathbf{x}) = \left\{ \begin{array}{l} 1.5 - k_b \\ 1.5V_{max} - V_{flutter} \\ \theta_{wing} \\ 3R_{crit} - R \end{array} \right\} \leq 0 & (10)
 \end{aligned}$$

#### 4. Results and discussion

Results of the large deformation bending test of the thin composite materials reveal the required folding constraints for the optimization. Fig. 5 shows the maximum radius at failure measured by DIC for different specimen thickness and hence the sharpest folding transition possible with the used material. Intuitively, as the thickness increases, the critical folding radius increases. Overall, especially the 1-ply specimen shows outstanding flexibility failing at radii below 3 mm. Here the outstanding flexibility of thin composite shells becomes evident, which was also observed by other researchers [31,18]. Fig. 5 also directly correlates feasible scale and geometry requirements of modern airfoils with the observed results. Airfoil shape, as well as minimum chordlength of the wing dictate the required critical bending radii, which are commonly found in the nose-section of the wing. Using the scale of research UAVs [29,27], small scale airborne wind energy drones [32] or fixed-wing VTOL aircraft [5,6], chord lengths of

Table 2  
Material properties (wing span (s) and chord (c) direction for CFRP).

	Strength $\sigma_s / \sigma_c$ [MPa]	Stiffness $E_s / E_c$ [GPa]	Density [g/cm <sup>3</sup> ]
CFRP twill	383.0/ 383.0	16.7/ 16.7	1.60
CFRP UD	2103.0/ 56.5	140.0/ 9.8	1.60
CFRP rods	1700.0	115.0	1.65
PLA ribs	50.0	3.5	1.30
Adhesive	30.2	-	1.04

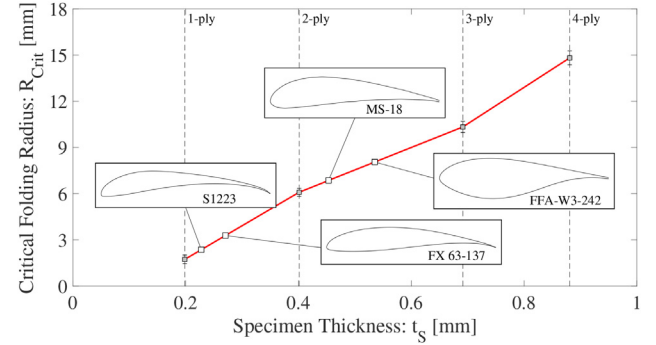


Fig. 5. Critical folding radius  $R_{crit}$  over specimen thickness and minimum radius of four representative high-lift airfoils with 300 mm chord length (No safety factors included). The error bars show the standard deviation of the sample. Eight samples per thickness were tested.

300 mm can be found. Scaling the respective high-lift low Reynolds number airfoils like the S1223 and the FX 63-127 [33] to the desired chord lengths and comparing them to the critical radius obtained from the platen folding tests reveals that 1-ply layups can be utilized in the nose-section, whereas for thicker airfoils like the MS-18 [34] or the wind turbine airfoil FFA-W3-242 [35] even 2-ply layups are possible to be used in the nose-section without failure.

Fig. 6 shows the resulting Moment-Curvature relation for each specimen thickness, visualizing the effort required to fold a flat sheet into a desired shape. As the curvature increases, the required folding moments increase drastically. Interestingly, the low thickness of the 1-ply samples allow for much higher bending moments, as they are able to withstand large curvatures without failure. For thicker specimen (3- and 4-ply) this size effect vanishes and the specimen begin to fail at a constant bending moment. The sharp transitions in the nose section can be easily folded by 1-ply specimen, showing only low bending moments for radii between 5 mm and 10 mm. It shall be noted, that the required folding moments scale linearly with the span, limiting the folding step to smaller spans  $\sim 3m$ . To achieve larger spans, piecewise folding and assembly can be envisioned.

The wing that is optimized has a rectangular planform with a chord length of 300 mm and a span of 1800 mm, similar to existing research UAV wings [29,27]. The chosen airfoil is a MS-18 high-lift, mild-stall airfoil, beneficial for high-lift application as it allows to relax speed safety margins and extends the allowable range of flight lift coefficients [34]. This airfoil, with a chordlength of 300 mm, allows 1- or 2-ply layups in the nose-section. However, the strengthening effects of thin carbon composite shells in high deformation bending are still a current research topic, necessitating a choice of large safety factors ( $S \geq 3$ ) with regards to folding induced strains. This shall account for unknown effects of material scatter or environmental influences. The maximum number of plies in the other sections are constrained considering the local curvature. Within the optimization, the maximum load factor of the wing is assessed using the aforementioned fluid structure interaction simulation. A linear buckling analysis is conducted, applying the aerodynamic loads flying at  $V_{max} = 50$  m/s with an angle of attack of  $\alpha = 8^\circ$ , which is a representative limit load for

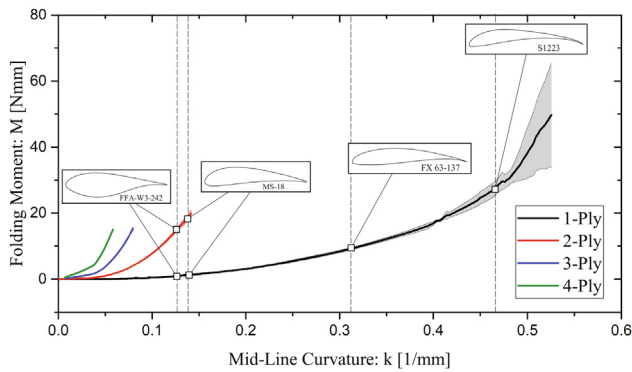


Fig. 6. Resulting folding moment for a 40 mm wide specimen with different specimen ply-counts for a different mid-line curvatures during the platen test. The shaded areas indicate the standard deviation of the sample. The marked points indicate the required folding moments for the realization of the shown airfoils at 300 mm chord length.

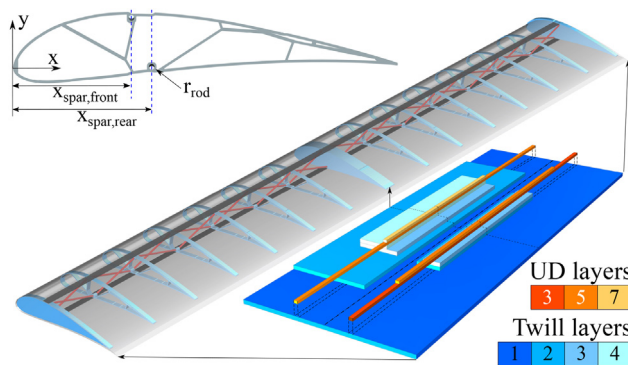


Fig. 7. Wing structure with detailed rib geometry and final composite layup thickness distribution.

state-of-the-art high lift fixed-wing UAVs, like small scale AWE drones [23].

The optimized wing with the Voronoi-rib and the composite layup thickness is shown in Fig. 7. The wing reaches a maximum load factor of  $n_{max} = 103.6$  at limit load, clearly exceeding the maximum wing load factor of conventional wingbox designs such as the Global Hawk UAV wing with  $n_{GH} = 29.1$  or the NASA undeflected Common Research Model wingbox with  $n_{uCRM} = 28.4$  (the estimation of these load factors are discussed in the appendix). The number of ribs is  $N_{ribs} = 15$  and the truss distribution given by the Voronoi parametrization shows distinct properties: the thin trailing edge is reinforcing to prevent decambering at high loads and the leading edge is stiffened with support trusses. The CFRP rods, replacing the spars, have a diameter of 4 mm, are placed close to each other and thereby form a wing box with the UD sparcaps. The center of the wingbox is placed so that the shear center of the wing is exactly at the aerodynamic center of pressure. Thereby, pure bending of the wing is achieved when applying aerodynamic loads. Depending on the application, the wing box and layup can be moved and adjusted to achieve desired wing twisting, for example tailoring the response to achieve twist down at large loads and thereby decreasing the wingtip angle of attack to reduce the root bending moment. The overall large number of ribs is required to prevent the thin wing skin from buckling and increase the torsional stiffness of the wing. An increase in the number of ribs decreases the size of the buckling fields, while also locally increasing the thickness of the skin, thereby adding to the overall torsional stiffness.

Apart from the rib and spar structure, the layup thickness distribution, which resulted from the aerostructural optimization, is shown in

Fig. 7. The load carrying capability is ensured by reinforcing the upper skin with a maximum of three additional twill layers, preventing the skin to buckle. Additionally, a comparably thick sparcap is added by the optimizer with a maximum of seven UD layers at the wingroot. The only region where the folding concept is limiting the design space is at the leading edge, where the layup is constrained to 1-ply. Apart from the sharp leading edge region, the optimizer can choose comparably thick laminates, still complying with the critical folding radius, as in these regions smooth shape transitions with small curvature are present.

The mass contribution of the individual components is shown in Fig. 8. It is noticeable that the wing skin accounts for 56% of the total mass, which results from the replacement of a conventional spar with the rod-rib concept which requires the integration of the load carrying and rather heavy spar-caps in the skin. Although the number of ribs is high, the low density of the 3D-printed PLA prevents excessive mass addition.

In Fig. 9, the strains induced by the folding and by the aerodynamic loading at the wing root section, where the highest strains occur, are shown. It can be seen that the folding induces highest strains in the leading edge at the maximum curvature, whereas the maximum strain induced by the aerodynamic loads is found around the thickest point of the airfoil. The strains induced by folding (1.1%) are far from the achieved maximum strains in the experiments ( $\epsilon_{fold} = \frac{1}{R_{crit}} \cdot \frac{t_s}{2} = 5.8\%$ ). It can also be seen that the aerodynamics induced strains are much lower than the folding strains, which is due to the buckling constraint that drives the design of the wing. However, even for higher aerodynamic induced strains, Fig. 9 nicely shows that the folding does not interfere with the aerodynamics induced strains, as the maximum strains occur at different locations on the airfoil.

The optimization results show the great applicability of the folding concept, especially for smaller scale structures (up to  $\sim 3$  m span), where folding moments are comparably low and the design of the wing is only limited by the folding constraints within the leading edge region. Nevertheless it shall be noted, that leading edge thicknesses of 0.2 mm also pose challenges with regard to handling and impact damage. Although safety factors with respect to folding induced loading are high, impact load cases (e.g. birdstrike) might damage the thin structure and require further investigations. However, especially for rapid design iterations or verification of experimental concepts at the scale of small to medium UAVs, the design concept offers a powerful prototyping alternative to classical 3D printing or mold lamination. In the following chapter, an experimental demonstrator based on the optimized wing structure is manufactured and tested to demonstrate its load carrying capability.

## 5. Validation: Manufacturing and testing of a folded wing structure

The optimized wing is manufactured according to the results of the aeroelastic optimization. A folding mechanism is designed to wrap the flat wing skin around the internal structure. The folding mechanism is composed of three parts, hinged in two places, to enable the stepwise positioning and folding of the skin around the internal structure, shown in Fig. 10. Each part is made of lasercut medium-density fibreboard (MDF) plates, connected in spanwise direction by steel profiles for additional stiffness. The detailed folding mechanism is shown in the appendix in Fig. 15.

The wing skin is cured in a flat state, rendering a complex mold unnecessary and simplifying the precise placement of the CFRP patches according to the results of the optimization. The internal ribs are additively manufactured on a commercially available 3D printer. Additive manufacturing of the ribs is ideal, given the geometric complexity of the rib. The spars are made of 4 mm diameter pultruded circular CFRP rods and are connected to the ribs with epoxy adhesive 3M

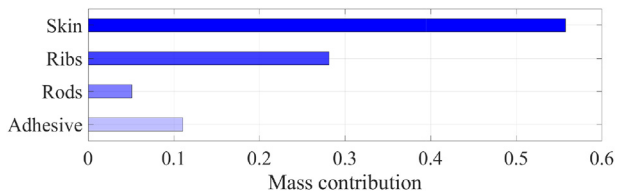


Fig. 8. Mass contribution of different wing components.

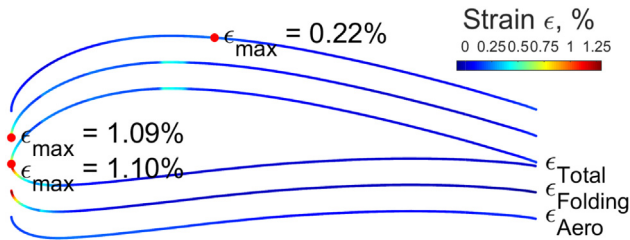


Fig. 9. Maximum strains at the wing root airfoil section induced by the folding loads, by the aerodynamic loads, and the total maximum strains.

DP490. The internal structure skeleton, consisting of the ribs and the spar rods, is assembled in a preliminary step before incorporating it into the skin. The skin is placed into the lower part of the folding mechanism, onto which the internal structure is bonded. The internal structure is temporarily clamped to the folding mechanism to keep it in place and prevent movement in relation to the skin and the mechanism itself. The front and top part of the mechanism are then folded around the internal structure (Fig. 10), thereby enclosing the ribs in the skin. By clamping the top and bottom parts of the folding mechanism, pressure is applied during the bonding process. In order to distribute the pressure uniformly, an elastic silicone film is placed between the folding mechanism and the skin. At the trailing edge of the wing, the top and bottom skin are bonded together to close the airfoil profile. After curing the adhesive, the mechanism is unfolded and the final wing is removed.

The adhesive connection between skin and ribs as well as the connection of the skin at the trailing edge was investigated after structural testing by sectioning the wing at random positions, which revealed high quality of the bonding process. Layup transitions between multiple weave layers as well as the noticeably thicker spar-caps could be found at their intended location with respect to the AM ribs, revealing a successful folding process.

The wing has a mass of 1.170 kg, compared to 1.047 kg from the simulation. A perfect bond was assumed between the skin and the ribs in the simulations, therefore, if the same mass of the adhesive as in the manufactured demonstrator is considered, the total mass is 1.177 kg in the simulation resulting in a mass variation of less than 1%.

The surface of the wing has an excellent quality, since the skin was laminated on a flat mirror-like surface, leading to a perfectly smooth aerodynamic surface. This is usually only achieved with expensive molds of highest surface quality. For prototyping and small series aerodynamic structures, the proposed concept is therefore a cost-effective alternative to existing manufacturing techniques.

In addition to the great correlation of the mass properties and the excellent surface quality, the shape of the airfoil was analysed. The shape of the skin was measured from various angles using a DIC system, and stitched together to get a full model of the airfoil. The resulting shape was compared to the initial MS-18 airfoil and combined in Fig. 11 for measurements of 20 mm width, taken at 200 mm and 450 mm from the wingtip. The standard deviation was calculated with a minimum of 8 measurement points in spanwise direction. The largest offset is observed at the hinge locations of the folding mechanism (Fig. 15), where the shape of the folding mechanism is interrupted by the hinges. A maximum orthogonal offset of 0.6 mm was recorded in the lower skin, with no sharp gradients. Although more detailed studies are required to determine the aerodynamic impact of the minor shape deviations, the perfectly smooth aerodynamic surface allows laminar flow conditions [36]. Also, the shape deviations in this prototyping study are lower or comparable to data from differentially manufactured composite aircraft structures (maximum manufacturing deviation reported between 0.5 mm–1 mm), which suffer from mold spring-in, stringer induced waviness and assembly deviations [37,38], but higher than for complex integrally manufactured mold-based concepts (maximum manufacturing deviation ~0.2 mm) [39].

In order to evaluate the load carrying capabilities of the manufactured wing and to validate the simulations, the wing is tested with a wing up-bending test, representing the case of limit loads. The limit load taken from the simulation results in a root bending moment of 215 Nm, and a lift force of 1064 N. A whiffletree was utilized to distribute the load at the location of the ribs, as shown in Fig. 12. By adjusting the geometry of the whiffletree, the distribution of the bending moment, shear, and torsion obtained from the aeroelastic analysis are matched closely. The shear, moment and torsion distribution along the wingspan (referred to the leading edge) is shown in Fig. 16 in the appendix, for the aerodynamic loads and the loads applied by the whiffletree.

The global displacement of the lower wing skin was measured using a DIC system, and compared to the numerical simulation. The

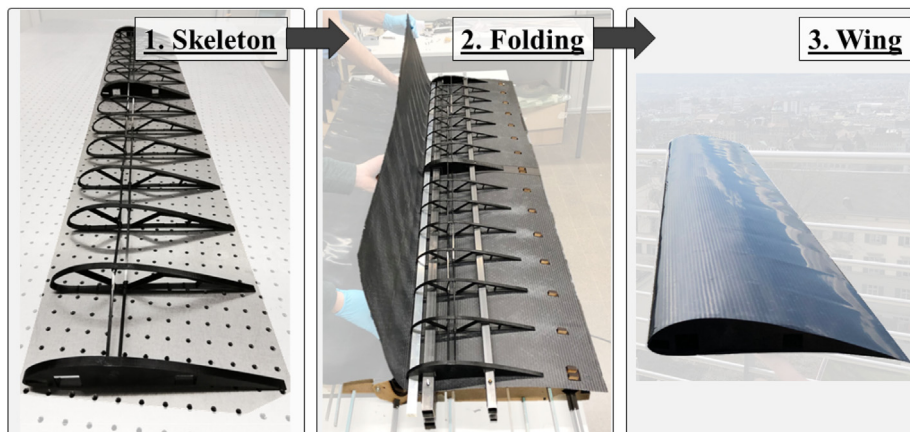


Fig. 10. Folding process, starting from the skeleton like internal structure and flat skin to the final wing structure.

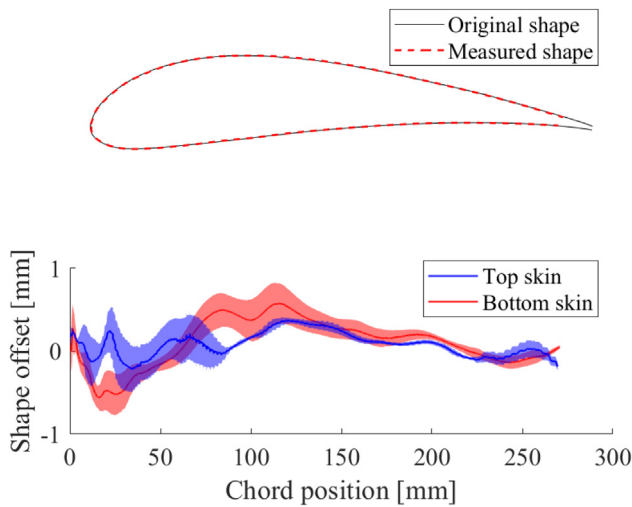


Fig. 11. Comparison between original and measured airfoil shape and orthogonal offset on upper and lower skin. The standard deviation was determined from a minimum of 8 measurement points in spanwise direction.

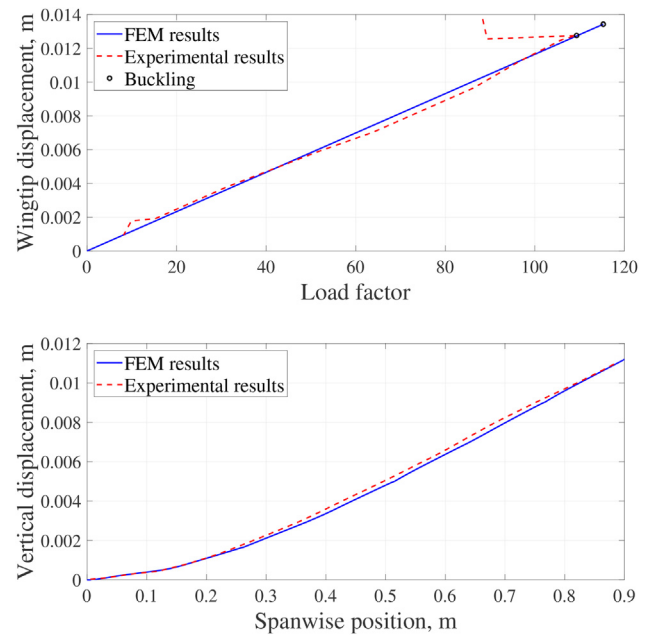


Fig. 13. Experimental results of the wing-up bending test. Top: The wing tip displacement as a function of load factor. Bottom: Wing deformation at a load factor of  $\frac{F}{mg} = 100$  as a function of the spanwise coordinate.

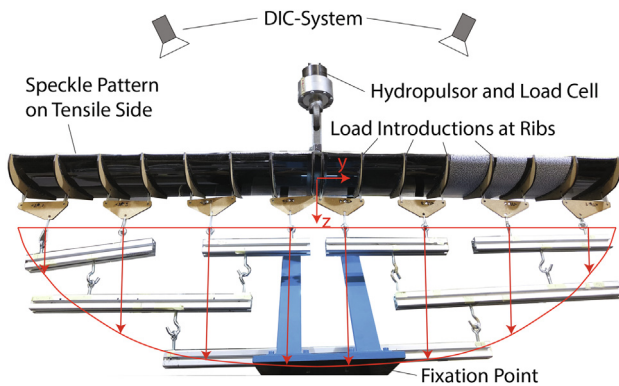


Fig. 12. Experimental setup of the wing-up bending test. The loads are distributed using an aluminum whiffletree and introduced via MDF load introduction elements attached to the wing at the rib locations.

vertical displacement of the lower wing surface along the spar was compared to the bending line obtained from the simulations. An excellent agreement was achieved, with a maximum deviation of 0.5 mm at the wingtip, shown in the bottom plot of Fig. 13. After the limit load test, the wing was tested up to failure. The wing failed at an ultimate load of 1255 N, where buckling occurred at the wing root upper skin, representing a load factor of 109.3. The buckling safety factor was set to 1.5 in the simulation, therefore, failure due to buckling was expected to occur at a load of 1596 N. The mismatch of 21% can be explained due to the UD-laminate thickness deviation of approximately 20–30%, induced by excessive bleeding of the thin UD prepregs in the manufacturing process. This led to a stiffness reduction in the spar caps and to the reduced strength of the wing. The simulation was adapted to the measured skin thickness for comparison with the experimental results. In Fig. 14, the comparison of the linear buckling analysis with the wing up bending test up to failure is shown. It can be seen that a very good agreement of the failure mode is achieved, with a mismatch of the buckling load of 5%.

These results validate the exceptional load carrying capability of the proposed structural concept. The folding induced stresses are not impairing the load carrying capability of the wing, as the maximum folding stresses occur in the leading edge region, whereas the aerodynamic loads induced stresses are mainly absorbed in the spar caps, as shown in Fig. 9.

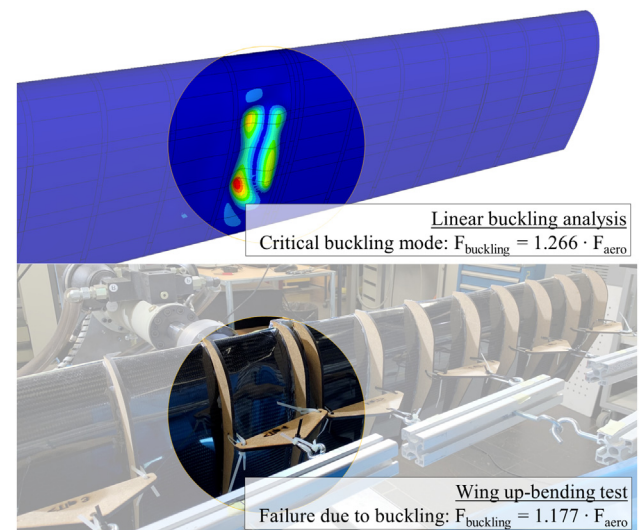


Fig. 14. Comparison of the simulated and experimental failure mode. Top: Linear buckling analysis. Bottom: Wing up bending test.

The results of the wing up-bending test highlight the suitability of the folding concept for high load carrying structures, achieving the predicted load factor of 100, without failure.

## 6. Conclusion

This study presents a design and manufacturing concept successfully bridging the gap between high load carrying composite structures and additive manufacturing. The concept is based on the folding of cured, thin composite-shells around additively manufactured core topologies, allowing to manufacture highly complex, mold-free structures. The load carrying capability is demonstrated on an optimized high-lift UAV wing. The wing withstands a load factor higher than 100, showing the potential of the developed concept. The study suc-

cessfully reveals that – especially for smaller scale wing structures such as for UAV's – the folding induced stresses during the forming of the complex geometry do not influence the load carrying capability or the design of the structure. The outstanding flexibility of thin composite shells allows for sharp geometry transitions without failure or excessive folding moments. Once curved, the shells show high load carrying capability and considerable stiffness in spanwise direction. Especially for cylindrical developable surfaces like the UAV wing considered in this study, this opens up new possibilities in the efficient prototyping of these otherwise labor and cost inefficient structures. Apart from the high load carrying capability, the wing exhibits a perfectly smooth aerodynamic surface and an excellent shape accuracy, highlighting the suitability for rapid prototyping in aerodynamic applications. To further investigate the suitability of the concept, also for long-term use, open questions like the susceptibility to impact damage need to be resolved. With additional three dimensional geometric complexity like for example wing twist, taper or airfoil changes, the design has to additionally ensure the developability of the wing skin. This additional constraint however can successfully be included into the design, using modern approaches of differential geometry which opens up new possibilities for multidisciplinary optimization, especially when linking aerodynamics with manufacturability.

While this study still uses conventional adhesive between the different structural components, it can be envisioned to use thermoplastic composite shells as skin elements, allowing to connect the skin and the internal structure in a fusion bonding process. This would further increase the lightweight characteristics and improve the design. Also, the process is not limited to wing structures, but can potentially replace complex high load carrying primary structures in robotics, automotive or other industries.

## 7. Author contributions

A.S, U.F and D.K contributed equally to this paper. A.S, U.F and D.K developed the concept, designed and manufactured the specimen and structures. All authors analyzed and discussed the data, contributed in writing, reviewing and editing of the manuscript. P.E supervised the study.

## Data availability

The datasets generated by study are available on request. Requests should be addressed to A.S or P.E.

## Declaration of Competing Interest

The authors declare that they have no known competing financial interests or personal relationships that could have appeared to influence the work reported in this paper.

## Acknowledgements

This research was funded by the ETH council Strategic Focus Area “Advanced Manufacturing” under the “AM-CFRP” initiative. The authors also acknowledge the SNF R'Equip program, SNF206021\_150729 “Optical measurement of three-dimensional surface displacement fields of morphing structures”, that has supported the acquisition of the Digital-Image-Correlation equipment.

## Appendix A. Appendix

### A.1. Folding mechanism

Fig. 15 shows the folding mechanism of the structure. It consists of MDF lasercut profiles, which were positioned at the PLA rib locations.

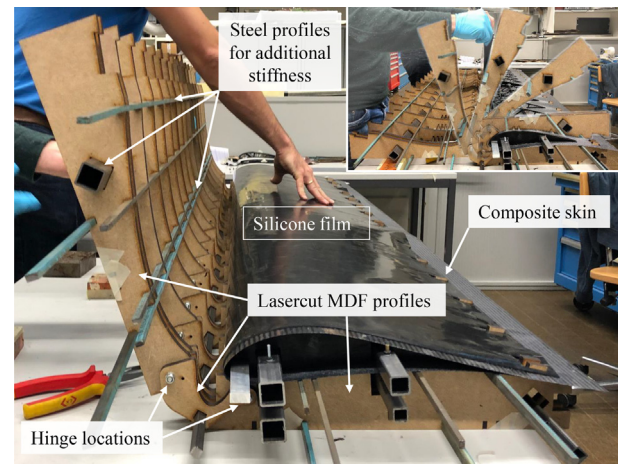


Fig. 15. Folding mechanism consisting of three hinged elements, connected through steel bars along the span.

The profiles were connected in spanwise direction by multiple steel beams to stiffen and align the construction. The lasercut profiles on the top and bottom side are connected close to the leading edge by two hinges. This allows the folding mechanism to exactly conform to the rib-shape, pressurizing the layup onto the PLA ribs. To ensure a uniform pressure distribution along the ribs and span, a 1 mm thick silicone film was placed in between the layup and the MDF profiles. To prevent the ribs and layups from slipping with respect to each other, the 3D-printed ribs were fixed by steel profiles, which were fitted into the rib geometry. Cutouts in the composite skin (done with a Zund NC-cutter) were introduced to align the wing skin with the MDF profiles at the trailing edge of the airfoil profile. Once folded and the adhesive had cured, the excess skin at the back (containing the cutouts) could be removed.

### A.2. Forces and moments applied by the aerodynamic and the whiffletree loads

Fig. 16 shows the shear, moment and torsion distribution along the wingspan for the aerodynamic loads (aero) and the loads applied by the whiffletree (equiv.). It can be seen that they match closely and the approach to evaluate the load carrying capabilities of the manufactured wing by a wing up-bending test is appropriate.

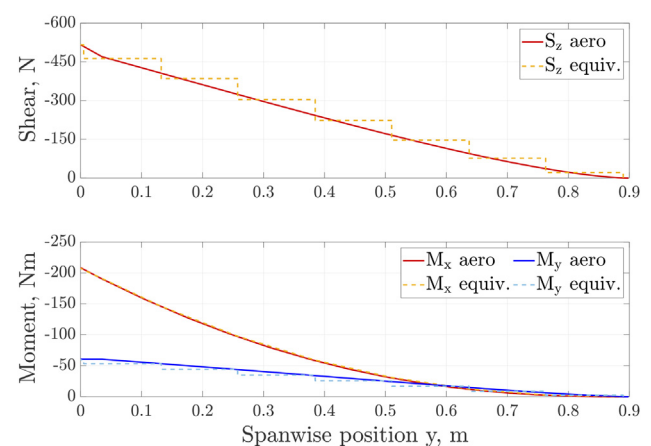


Fig. 16. Shear ( $S_z$ ), bending ( $M_x$ ) and torsion ( $M_y$ ) distribution. Aerodynamic loads (aero) and whiffletree loads (equiv.).

### A.3. Load factor of conventional wings

The wing introduced in this study reaches a maximum load factor of  $n_{max} = 103.6$  at limit load. This is remarkable compared to the maximum wing load factor of conventional wingbox designs such as the Global Hawk UAV wing ( $n_{GH} = 29.1$ ) or the NASA undeflected Common Research Model wingbox ( $n_{uCRM} = 28.4$ ). The Global Hawk UAV load factor is calculated as follows: the UAV has a maximum take-off weight of 11612 kg, a wing structural weight of 998 kg, and is designed considering a 2 g vertical load with a safety factor of 1.25 [40]. This results in a wing load factor of  $n_{GH} = 29.1$ . For the NASA undeflected Common Research Model uCRM-13.5, which is a numerical model with similar dimensions and structural topology to that of the Boeing 777, the maximum take-off weight is 284,256 kg. The wingbox structural weight is 1.25 · 30,032 kg (the factor of 1.25 accounts for additional weight associated with fasteners, overlaps, and other components not modeled in the idealized wingbox) and is designed considering a critical 2.5 g pull-up maneuver with a safety factor of 1.5 [41]. This results in a maximum wing load factor of  $n_{uCRM} = 28.4$ .

### References

- [1] Njuguna J. Lightweight composite structures in transport; 2016..
- [2] Witik RA, Payet J, Michaud V, Ludwig C, MÖnson JAE. Assessing the life cycle costs and environmental performance of lightweight materials in automobile applications. *Compos Part A Appl Sci Manuf* 2011;42(11):1694–709. <https://doi.org/10.1016/j.compositesa.2011.07.024>.
- [3] Giones F, Brem A. From toys to tools: The co-evolution of technological and entrepreneurial developments in the drone industry. *Bus Horizons* 2017;60(6):875–84. <https://doi.org/10.1016/j.bushor.2017.08.001>.
- [4] Ahrens U, Diehl M, Schmehl R. Airborne wind energy. *Green Energy Technol*. doi: 10.1007/978-3-642-39965-7..
- [5] Johnson W, Silva C, Solis E. Concept vehicles for VTOL air taxi operations. In: *Proceedings of the AHS international technical meeting on aeromechanics design for transformative vertical flight*.
- [6] Silva C, Johnson W, Antcliff KR, Patterson MD. VTOL urban air mobility concept vehicles for technology development. In: 2018 Aviation technology, integration, and operations conference. p. 1–16. <https://doi.org/10.2514/6.2018-3847>.
- [7] Goh GD, Agarwala S, Goh GL, Dikshit V, Sing SL, Yeong WY. Additive manufacturing in unmanned aerial vehicles (UAVs): challenges and potential. *Aerosp Sci Technol* 2017;63:140–51. <https://doi.org/10.1016/j.ast.2016.12.019>.
- [8] Eichenhofer M, Wong JC, Ermanni P. Continuous lattice fabrication of ultralightweight composite structures. *Addit Manuf* 2017;18:48–57. <https://doi.org/10.1016/j.addma.2017.08.013>.
- [9] Fasel U, Keidel D, Baumann L, Cavolina G, Eichenhofer M, Ermanni P. Composite additive manufacturing of morphing aerospace structures. *Manuf Lett*. doi: 10.1016/j.mfglet.2019.12.004..
- [10] Krivoshapko SN, Shambina S. Design of developable surfaces and the application of thin-walled developable structures. *Serbia Arch J*. p. 4. doi: 10.1115/1.2885509, URL:<http://saj.rs/wp-content/uploads/2016/11/SAJ-2012-03-S-N-Krivoshapko-S-Shambina.pdf>..
- [11] Mallikarachi HMYC, Pellegrino S. Design of ultrathin composite self-deployable booms. *J Spacecr Rockets* 2014;51(6):1811–21. <https://doi.org/10.2514/1.A32815>. URL:<http://arc.aiaa.org/doi/10.2514/1.A32815>.
- [12] Schlothauer A, Ermanni P. Stiff composite cylinders for extremely expandable structures. *Sci Rep* 2019;9(1):1–8. <https://doi.org/10.1038/s41598-019-51529-7>.
- [13] Lawrence S. Developable surfaces: their history and application. *Nexus Network J* 2011;13(3):701–14. <https://doi.org/10.1007/s00004-011-0087-z>.
- [14] Bo P, Zheng Y, Zhang C. Smooth quasi-developable surfaces bounded by smooth curves. *arXiv:1905.07518*. <http://arxiv.org/abs/1905.07518>.
- [15] Sun M, Fiume E. Technique for constructing developable surfaces. In: *Proceedings - graphics interface*: 1996. p. 176–85..
- [16] Tang C, Bo P, Wallner J, Pottmann H. Interactive design of developable surfaces. *ACM Trans Graph* 35 (2). doi: 10.1145/2832906..
- [17] Murphey TW, Peterson ME, Grigoriev MM. Large strain four-point bending of thin unidirectional composites. *J Spacecr Rockets* 2015;52(3):882–95. <https://doi.org/10.2514/1.A32841>. <http://arc.aiaa.org/doi/10.2514/1.A32841>.
- [18] Murphey TW, Francis W, Davis B, Mejia-Ariza JM. High strain composites. In: 2nd AIAA spacecraft structures conference; 2015. p. 1–53. doi: 10.2514/6.2015-0942, URL:<http://arc.aiaa.org/doi/10.2514/6.2015-0942>..
- [19] Reu P. All about speckles: speckle density. *Exp Tech* 2015;39(3):1–2. <https://doi.org/10.1111/ext.12161>.
- [20] Timoshenko SP, Gere J. Theory of elastic stability; 1963. doi: 10.1115/1.3636481..
- [21] Sanford G, Biskner A, Murphey T. Large strain behavior of thin unidirectional composite flexures. In: *Proceedings of the 51st AIAA/ASME/ASCE/AHS/ASC structures, structural dynamics, and materials conference*, no. April; 2010. doi: 10.2514/6.2010-2698, URL:<http://arc.aiaa.org/doi/pdf/10.2514/6.2010-2698>..
- [22] Molinari G, Arrieta AF, Ermanni P. Aero-structural optimization of three-dimensional adaptive wings with embedded smart actuators. *AIAA J* 2014;52(9):1940–51. <https://doi.org/10.2514/1.J052715>. <http://arc.aiaa.org/doi/abs/10.2514/1.J052715>.
- [23] Fasel U, Tiso P, Keidel D, Molinari G, Ermanni P. Reduced-order dynamic model of a morphing airborne wind energy aircraft. *AIAA J* 2019:1–13. <https://doi.org/10.2514/1.J058019>.
- [24] Hansen N, Ostermeier A. Completely derandomized self-adaptation in evolution strategies. *Evol Comput* 2001;9(2):159–95. <https://doi.org/10.1162/106365601750190398>.
- [25] MSC Software Corporation. MSC Nastran Linear Static Analysis User's Guide; 2014..
- [26] Hodges DH, Pierce GA. Introduction to structural dynamics and aeroelasticity. Cambridge University Press; 2002.
- [27] Molinari G, Arrieta AF, Guillaume M, Ermanni P. Aerostructural performance of distributed compliance morphing wings: wind tunnel and flight testing. *AIAA J* 2016;54(12):3859–71. <https://doi.org/10.2514/1.J055073>.
- [28] Hamda H, Jouve F, Evelyne L, Schoenauer M, Sebagn M. Compact unstructured representations for evolutionary design. *Appl Intell* 2002;16(2):139–55.
- [29] Keidel D, Molinari G, Ermanni P. Aero-structural optimization and analysis of a camber-morphing flying wing: Structural and wind tunnel testing. *J Intell Mater Syst Struct* 2019;30(6):908–23. <https://doi.org/10.1177/1045389X19828501>.
- [30] Fasel U, Keidel D, Molinari G, Ermanni P. Aerostructural optimization of a morphing wing for airborne wind energy applications. *Smart Mater Struct* 26 (9). doi: 10.1088/1361-665X/aa7c87..
- [31] Yee J, Pellegrino S. Biaxial bending failure locus for woven-thin-ply carbon fibre reinforced plastic structures. In: 46th AIAA/ASME/ASCE/AHS/ASC structures, structural dynamics and materials conference (April); 2005. p. 1–8. doi: 10.2514/6.2005-1811, URL:<http://arc.aiaa.org/doi/10.2514/6.2005-1811>..
- [32] Keidel D, Fasel U, Baumann L, Molinari G, Ermanni P. Experimental validation of a morphing wing for airborne wind energy applications. In: 28th Int. conf. adapt. struct. technol. Cracow, Pol.; 2017. p. 1–11..
- [33] Selig MS, Guglielmo JJ. High-lift low Reynolds number airfoil design. *J Aircraft* 1997;34(1):72–9. <https://doi.org/10.2514/2.2137>.
- [34] Nagel A, Shepshelovich M. The concept of high-lift, mild stall wing. In: 24th International congress of the aeronautical sciences, vol. 29; 2004..
- [35] Bjorck A. Coordinates and calculations for the FFA-W1-xxx, FFA-W2-xxx, FFA-W2-xxx and FFA-W3-xxx series of airfoils for horizontal axis wind turbines. *Tech. rep*; 1990..
- [36] Holmes BJ, Obara CJ, Martin GL, Domack CS. Manufacturing tolerances for natural laminar flow airframe surfaces. *SAE Tech Pap* 1985;94(1985):522–31. <https://doi.org/10.4271/850863>.
- [37] Makinde OM, de Faria AR, Donadon MV. Prediction of shape distortions in composite wing structures. *Latin Am J Solids Struct* 15 (11MecSol2017Joinville):2018;1–15. doi: 10.1590/1679-78254295..
- [38] Anderson A, Longo C, Teufel P. New composite design and manufacturing methods for general aviation aircraft structures. In: 24th International congress of the aeronautical sciences; 2004. p. 1–12..
- [39] Heinrich L, Kruse M. Laminar composite wing surface waviness – two counteracting effects and a combined assessment by two methods. *Deutscher Luft- und Raumfahrtkongress* 2016;2016(7):1–10.
- [40] Gundlach JF. Multidisciplinary design optimization of subsonic fixed-wing unmanned aerial vehicles projected through 2025. Ph.D. thesis, Virginia Tech; 2004..
- [41] Brooks TR, Kenway GK, Martins JR. Benchmark aerostructural models for the study of transonic aircraft wings. *AIAA J* 2018;56(7):2840–55.